





## Discovery of a Dust Sorting Process on Boulders Near the Reiner Gamma Swirl on the Moon



### Key Points:

- In a catalog of lunar boulder images, we find a new type of reflectance feature associated with boulders
- The feature is likely a dust mantling with unique photometric properties
- Several formation scenarios are discussed

Ottaviano Rüsçh<sup>1</sup> , Marcel Hess<sup>2</sup> , Christian Wöhler<sup>2</sup>, Valentin T. Bickel<sup>3</sup>, Rachael M. Marshal<sup>1</sup> , Markus Patzek<sup>1</sup> , and Hans L. F. Huybrighs<sup>4,5,6</sup>

<sup>1</sup>Institut für Planetologie, Westfälische Wilhelm Universität Münster, Münster, Germany, <sup>2</sup>Image Analysis Group, TU Dortmund University, Dortmund, Germany, <sup>3</sup>Center for Space and Habitability, University of Bern, Bern, Switzerland, <sup>4</sup>Space and Planetary Science Center, Khalifa University, Abu Dhabi, UAE, <sup>5</sup>Department of Mathematics, Khalifa University, Abu Dhabi, UAE, <sup>6</sup>School of Cosmic Physics, DIAS Dunsink Observatory, Dublin Institute for Advanced Studies, Dublin, Ireland

### Correspondence to:

O. Rüsçh,  
ottaviano.ruesch@uni-muenster.de

### Citation:

Rüsçh, O., Hess, M., Wöhler, C., Bickel, V. T., Marshal, R. M., Patzek, M., & Huybrighs, H. L. F. (2024). Discovery of a dust sorting process on boulders near the Reiner Gamma swirl on the Moon. *Journal of Geophysical Research: Planets*, 129, e2023JE007910. <https://doi.org/10.1029/2023JE007910>

Received 19 MAY 2023

Accepted 21 DEC 2023

**Abstract** In a database of lunar fractured boulders (Rüsçh & Bickel, 2023, <https://doi.org/10.3847/psj/acd1ef>), we found boulders with reflectance features dissimilar to previously known morphologies. We performed a photo-geologic investigation and determined that the features correspond to a dust mantling on top of boulders with a unique photometric behavior. We next performed a photometric model inversion on the dust mantling using Bayesian inference sampling. Modeling indicates that the dust photometric anomaly is most likely due to a reduced opposition effect, whereas the single scattering albedo is not significantly different from that of the nearby background regolith. This implies a different structure of the dust mantling relative to the normal regolith. We identified and discussed several potential processes to explain the development of such soil. None of these mechanisms can entirely explain the multitude of observational constraints unless evoking anomalous boulder properties. Further study of these boulders can shed light on the workings of a natural dust sorting process potentially involving dust dynamics, a magnetic field, and electrostatic dust transport. The presence of these boulders appears to be limited to the Reiner K crater near the Reiner Gamma magnetic and photometric anomaly. This close spatial relationship further highlights that poorly understood processes occur in this specific region of the Moon.

**Plain Language Summary** The study of rocks on the surface of the Moon is important to understand the processes forming and modifying the lunar crust as well as the processes modifying rocks after their formation. The lunar rocks resting on the surface can be studied by imaging them with an orbital camera and analyzing their shape and reflectance. Here we report on the finding of a new type of brightness feature on rocks. This finding was made possible by scrutinizing a catalog of split lunar rocks. The brightness feature is found to be unique because of its rare occurrence, localization limited to near the Reiner Gamma magnetic anomaly, and association with some but not all rocks of the crater Reiner K. The feature is a dust deposit with a potentially uncommon physical structure.

## 1. Introduction

The surface of the Moon is littered with boulders (>25.6 cm, Dutro et al., 1989) and smaller rock fragments. In contrast to the comminuted, fine-grained and highly mixed regolith, the intact multi-crystals rocks preserve the minerals and components in their pristine size and spatial configuration, that is, the lithology formed by the magmatic, impact and impact-related sedimentary processes. These processes inform the properties and evolution of the Moon crust and mantle. Importantly, these rocks may have recorded the environmental conditions, such as the magnetic field, during their formation. Therefore, questions addressing the Moon core property and its dynamo can be addressed (e.g., Cisowski et al., 1983; Lawrence et al., 2008; Tarduno et al., 2021; Tikoo et al., 2017).

A large fraction of lunar boulders are emplaced as impact ejecta blocks (e.g., Bandfield et al., 2011; Melosh, 1989) and, after an exposure time of several millions to several tens of millions of years (e.g., Rüsçh et al., 2022), are shattered by impacts and reduced to regolith (e.g., Hörz & Cintala, 1997). During the period on the surface, exposure to the space environment can modify their surface and near sub-surface. Space weathered rocks develop patinas of impact glass (e.g., Keller et al., 1997; Wentworth et al., 1999), and a fine layer of dust on their surfaces (e.g., Johnson et al., 2014; Sun & Lucey, 2022). The latter will itself be subject to space weathering (e.g., Pieters

© 2024 The Authors.

This is an open access article under the terms of the [Creative Commons Attribution-NonCommercial License](https://creativecommons.org/licenses/by/4.0/), which permits use, distribution and reproduction in any medium, provided the original work is properly cited and is not used for commercial purposes.

**Table 1**

*Images Used in This Study With Their Respective Incidence Angle, Assuming a Flat Surface at the Center Pixel, Phase Angle at the Center Pixel, and Nominal Resolution*

Image ID	Incidence angle (RE) [deg]	Phase angle (RE) [deg]	Nominal resolution (RE) [m]
M109589691RE/LE	10.84	10.40	0.51
M1134551181RE/LE	16.44	15.55	0.92
M1200481033RE/LE	71.23	70.08	0.91
M1269886133RE/LE	7.30	7.36	0.92
M1285164183RE/LE	9.89	9.89	0.90
M1315723777RE/LE	15.61	14.76	0.72
M132003371RE/LE	84.80	83.67	0.87
M1374450022RE/LE	12.33	11.73	0.70

*Note.* The angles and resolution are given for the right image, respectively.

& Noble, 2016). Three processes likely contribute to the development of the dust layer: (a) accumulation of ballistic ejecta particles produced by impacts, (b) particle production by the rock itself due to micrometeoroid bombardment (e.g., Hörz et al., 1974; Rüsch & Wöhler, 2022) and to thermal fatigue (Patzek & Rüsch, 2022), and (c) deposition of electrostatically lofted dust particles (e.g., Rennilson & Criswell, 1973; Wang et al., 2016; Yan et al., 2019).

In a recent effort to understand lunar boulders using optical images from orbit, a catalog of boulders with specific (fragmentation) morphologies has been produced for the latitude range  $\pm 60^\circ$  (Rüsch & Bickel, 2023). The catalog was constructed from LROC/NAC images (Robinson et al., 2010) using a convolutional neural network architecture purposely trained on a wide range of degradation morphologies. As a result, detections in the catalog span a considerable range of morphologies not limited to stages of rock fragmentation. About a third of the catalog ( $n \sim 40,000$ ) was visually inspected in Rüsch and Bickel (2023). Besides the expected morphologies, the survey revealed one surprising fragmented boulder with unique characteristics, most importantly a very dark area at the center of fragments, unlike any known lunar

boulder morphologies (reported in e.g., Muelhberger et al., 1972; Florensky et al., 1978; Krishna & Kumar, 2016; Ruesch et al., 2020). We found only one such peculiar-looking boulder in the catalog, and we found its location to be at the impact crater Reiner K. These peculiarities motivated a detailed photo-geologic and photometric study. The detailed photo-geologic study focused on the Reiner K crater, and three large regions were scrutinized to search for additional occurrences. Here we report the outcomes of the analysis and discuss the implications for a new dust sorting process. Throughout this manuscript, we refer to the discovered feature as a photometrically anomalous dusty boulder (PADB).

## 2. Methods

### 2.1. Data Processing and Photo-Geology

The two Narrow Angle Cameras (NACs) onboard the Lunar Reconnaissance Orbiter (LRO) image the lunar surface under a variety of illumination conditions at a high resolution of 0.5 m/pixel at a nominal altitude of 50 km (Robinson, et al., 2010). To study the PADBs at the Reiner K crater, the images listed in Table 1 were used. These images were radiometrically calibrated with the Integrated Software for Imagers (ISIS) (Laura et al., 2022). Subsequently, the images were map projected with a common resolution of 1 m/pixel to the region of interest ( $8.02^\circ\text{N}$ – $8.17^\circ\text{N}$  latitude and  $305.93^\circ\text{E}$ – $306.08^\circ\text{E}$  longitude) using ISIS, and the left (L) and right (R) images of the two cameras were combined in a mosaicking step.

All images were then manually co-registered to the reference image M109589691. These images were used for photo-geological characterization based on visual inspection by experts. The visual inspection encompassed the characterization of the overall distribution of PADBs and normal boulders of the spatial extent of the dark area on PADB and the spatial relationship of the dark area to the shape of the underlying boulders.

To determine whether PADBs occur at locations other than Reiner K crater, we performed a visual search at and near the high reflectance region of Reiner Gamma, at and near the swirl Mare Ingenii, and at and near the swirl Gerasimovich using the swirl map of Denevi et al. (2016). In these three regions, the search task first encompassed the identification of craters not smaller than Reiner K (3 km), and as young as Reiner K, in order to ensure the formation of sufficiently large ejecta boulders and their presence in high abundance, respectively. The relative age between craters was based on morphological criteria (e.g., well-defined rim, presence of rays). Subsequently, low incidence angle images ( $<30^\circ$ ) were used to search for relatively dark spots on boulders and moderate incidence angle images ( $40$ – $80^\circ$ ) were used to verify a background brightness at the same locations.

The photometric investigation focused on the Reiner K crater. There, several types of features were identified, that is, PADBs, dark regolith, bright regolith (partly containing unresolved rock fragments), and normal boulders (with and without dust). For photometrical investigation, it was necessary to further refine the image co-registration in order to reach alignment at the pixel level over the entire region. Therefore, for each of the four feature types,

six representative locations were manually selected, and in each image, the corresponding pixel locations were refined and saved. Subsequently, for each selected pixel in each image, and for each location, the mean over the local neighborhood of 3 x 3 pixels was calculated. Additionally, for each location, the sub spacecraft and subsolar point, the spacecraft altitude and the solar distance were obtained using ISIS (Laura, et al., 2022). With this information and the longitude and latitude of that specific pixel the vector pointing to the sun ( $\vec{s}$ ) and to the spacecraft ( $\vec{v}$ ) were calculated. Based on this information, a photometric model was applied. Because the 3D-reconstruction of boulders is particularly challenging due to their albedo and topography, no Digital Terrain Model (DTM) was used. Instead, the inclination along the illumination direction (East-West) was considered as a parameter of the model and fitted for each location individually.

## 2.2. Photometric Model Inversion

The basis of the photometric modeling approach used in this work is the isotropic multiple scattering approximation (IMSA) of the Hapke (2012) model as outlined by Sato et al. (2014):

$$r(i, e, g) = \frac{w}{4\pi} \frac{\mu_{0,e}}{\mu_e + \mu_{0,e}} [p(g)B_{SH}(g) + H(\mu_e)H(\mu_{0,e}) - 1]S(i, e, \psi). \quad (1)$$

Here,  $w$  denotes the single scattering albedo, which describes how much light is scattered compared to how much light is absorbed. The incidence angle ( $i$ ) and the emission angle ( $e$ ) are corrected for the effects of roughness to obtain the effective angles ( $i_e, e_e$ ) and their respective cosines ( $\mu_{0,e} = \cos i_e, \mu_e = \cos e_e$ ) as well as the correction factor  $S(i, e, \psi)$ , which also depends on the azimuth angle  $\psi$ . For a detailed description of the roughness correction, see Hapke (2012) and Sato et al. (2014). The photometric roughness angle is set to  $11^\circ$  as derived as a global average by Warell (2004) because the effects of roughness are comparatively pronounced at large phase angles, while the observed variations occur mainly at small phase angles. The single particle phase function ( $p(g)$ ) depends on the phase angle  $g$  and the two-material-specific parameters  $b_h$  and  $c_h$ . In this work, the double Henyey Greenstein formulation is used.

$$p(g) = \frac{1 + c_h}{2} \frac{1 - b_h^2}{(1 - 2b_h \cos(g) + b_h^2)^{3/2}} + \frac{1 - c_h}{2} \frac{1 - b_h^2}{(1 + 2b_h \cos(g) + b_h^2)^{3/2}} \quad (2)$$

The parameters  $b_h$  and  $c_h$  are strongly correlated (Hapke, 2012) according to the hockey-stick relation given by:

$$c_h = 3.29 e^{(-17.4b_h^2)} - 0.908, \quad (3)$$

which is used in this work to calculate  $c_h$  for any given  $b_h$  value.

Multiple scattering within the medium is modeled with the Chandrasekhar H-functions using the approximation introduced by Hapke (2002). The opposition effects of shadow hiding, responsible for an increased brightness under small phase angles, and coherent backscattering are combined in the correction factor for shadow hiding  $B_{SH}$ , which comprises a width ( $h_s$ ) and an amplitude ( $B_{S0}$ ).

$$B_{SH}(g) = 1 + B_{S0} \frac{1}{1 + \tan(g/2)/h_s} \quad (4)$$

The amplitude of the effect is strongly correlated with the albedo. To account for this correlation, we used the relationship empirically estimated by Sato et al. (2014) for the LRO Wide Angle Camera (WAC) channels. The relationship determines the predicted value for a given albedo and parameters of the phase function:

$$B_{S0,p} = \frac{sw + t}{wp(0)}, \quad (5)$$

By dividing the estimated value by the predicted value, a corrected value  $B_{S0,c}$  was obtained that is independent of the albedo, and which can give insight into whether the opposition effect is stronger or weaker than usually found on the Moon. For example, a soil that has a  $B_{S0,c}$  value larger than one would have a stronger opposition effect compared to the average value for the given albedo and vice versa.

Given the photometric model and observations of the same location from different viewing and illumination conditions, the Hapke model needed to be inverted to obtain the parameters of the model. However, the inversion

might not have a unique solution (e.g., Hess et al., 2023; Schmidt & Fernando, 2015). To account for multiple equally likely solutions, we used Bayesian inference sampling (Bishop & Nasrabadi, 2006; Gelman et al., 1995) similar to Hess et al., 2023. In the Bayesian sense, all parameters of the model are described by probability distributions and are sampled from the so-called posterior distribution to obtain the most likely solution as well as the uncertainties. Solutions that fit similarly well are also accepted.

For each feature type, N locations were selected with similar visual properties. For each location, M images for different phase angles were acquired by the NAC. For each location a surface normal  $\vec{n}$  had to be determined. To reduce the degree of freedom without losing the important information for the reflectance model we varied the inclination angle ( $\Theta$ ) only along the East-West direction so that  $\vec{n}$  becomes:

$$\vec{n} = (\sin \Theta, 0, \cos \Theta) \quad (6)$$

The modeled values were then calculated with varying inclination angles for the N locations but with the same parameters for all locations of a feature type.

$$\vec{R}_{\text{refl}} = [\vec{r}_1(w, B_{S0}, b_h, c_h, \Theta_1), \dots, \vec{r}_N(w, B_{S0}, b_h, c_h, \Theta_N)] \quad (7)$$

with every  $\vec{r}_i(w, B_{S0}, b_h, c_h, \Theta_i)$  being a  $M \times 1$  vector. The N vectors  $\vec{r}_i$  for each location were then concatenated to form the vector  $\vec{R}_{\text{refl}}$ , which then has the length  $NM \times 1$ . Additionally, to better separate the effects of albedo and parameters which change the phase curve, phase ratio information was used. The vector for location  $i$  then becomes

$$\vec{r}_{\text{phase},i} = \log_{10}(\vec{r}_i(2 \dots M)/\vec{r}_i(1)) \quad (8)$$

and has the dimension  $(M - 1) \times 1$ . Concatenating these vectors to the end of the  $\vec{R}_{\text{refl}}$  vector resulted in a  $(2M - 1)N \times 1$  sized vector denoted  $\vec{R}_{\text{model}}$ . The likelihood function in the Bayesian model represents the quality of the fit between the modeled and measured ( $\vec{R}_{\text{meas}}$ ) values given a set of parameters. It was subsequently marginalized:

$$p(w, B_{S0}, b_h, c_h, \vec{\Theta}, \sigma_{\text{refl}}, \sigma_{\text{phase}}) \sim \prod_{k=1}^{(2M-1)N} N(\vec{R}_{\text{meas},k} | \mu = R_{\text{model},k}, \sigma = \sigma_{lh,k}) \quad (9)$$

where  $\sigma_{lh,k}$  was chosen as  $\sigma_{\text{refl}}$  or  $\sigma_{\text{phase}}$  depending on whether  $R_{\text{model},k}$  is a reflectance value or phase ratio information. The variance of the likelihood function is a parameter of the model, and because the phase ratio and reflectance values differ by several orders of magnitude, it is sensible to use two different parameters respectively. The priors were defined as listed in Appendix A. The sampling algorithm used was the No U-turn Sampler (NUTS) (Hoffman & Gelman, 2014) implementation in pymc3 (Salvatier et al., 2016), which is very efficient even for highly correlated parameters and high dimensional parameter spaces. For each feature type 20,000 samples were drawn, and 5,000 additional samples were created for tuning.

### 3. Results

#### 3.1. Geology

On the basis of reflectance alone, at the Reiner K crater, we identified 23 occurrences of 5–20 m large photometrically anomalous areas and ~200 smaller occurrences of <4 m in size (Figure 1). Each large photometrically anomalous area is spatially associated with one, and only one, boulder. When viewed at high incidence angle images, the area corresponds to a dust coverage on a boulder (Figures 2f–2i). We therefore refer to photometrically anomalous dusty boulders (PADB). In moderate to high incidence angle images, boulders with these features are similar to classical dust-covered boulders (Figures 2e–2j), that is, boulders whose top surface is partially covered by very finely grained regolith (e.g., Wolfe et al., 1981). This is probably the reason why these features have not been reported before in photo-geological studies that use moderate to high incidence angle images. PADBs are visually indistinguishable from non-PAD boulders, that is, they do not differ in terms of size (width, height) or shape. They neither show a preferential orientation of their shape or major axis with respect to the absolute selenographic orientation nor with respect to the source crater. PADBs are located at varying distances and azimuths from the crater center, with a concentration in the northwestern quadrant of the lunar

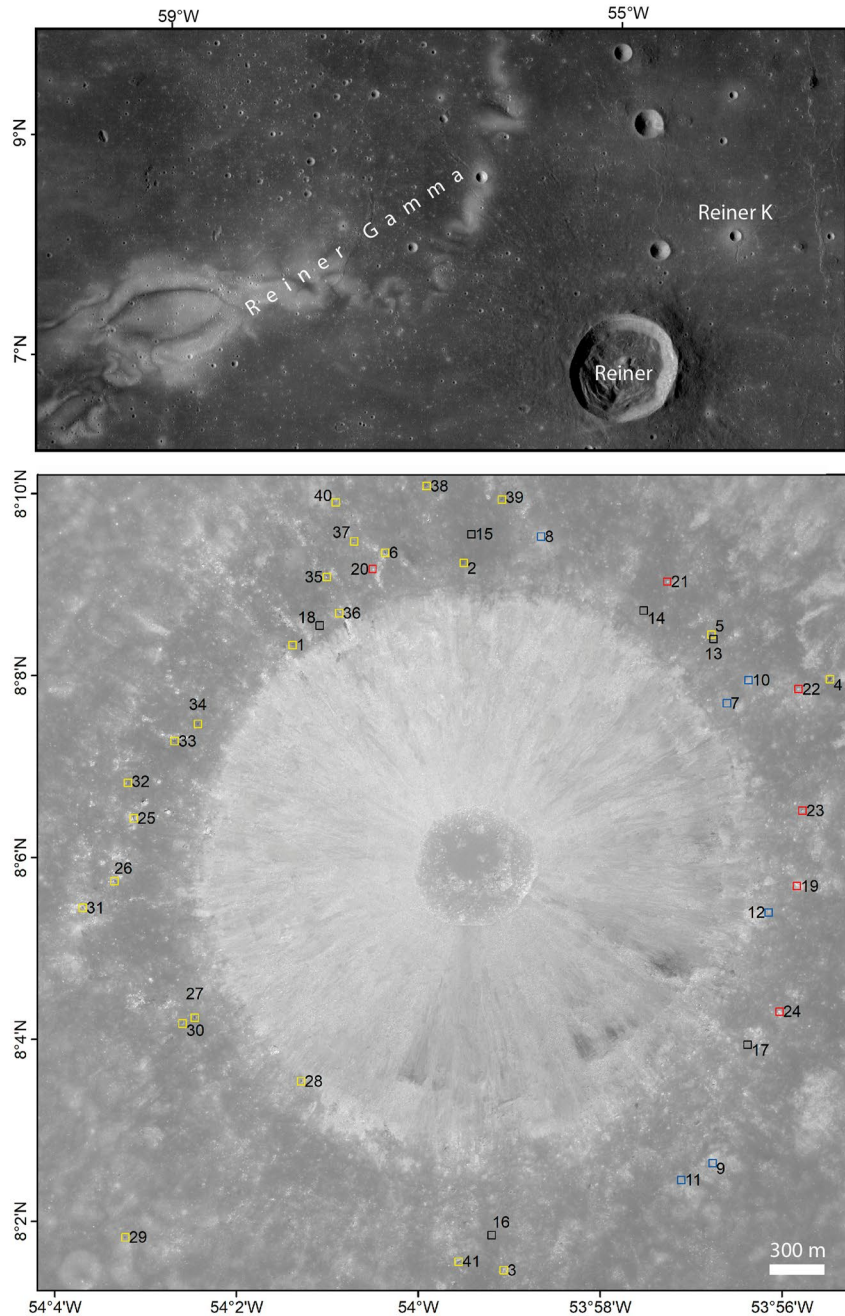


**Figure 1.** Upper panel: Context of the photometrically anomalous dusty boulders (PADB) near the magnetic anomaly of Reiner Gamma, visible as a bright swirl west of Reiner K. Lower panel: Locations used for the different feature types are overlaid on top of reference image M109589691. Large PADBs are marked in yellow, bright regolith in blue, dark regolith in black, and normal boulders in red.

nearside. Notably, the PADB spatial distribution around the crater mimics that of non-PADBs, although PADBs have a lower abundance compared with non-PADBs. In the northwestern quadrant (Figure 3), some PADBs are aligned with a radial orientation centered on the crater, typical for boulders formed as ejecta blocks. PADBs are not found at the crater floor. For all large PADBs, we observe that (a) the boundary of the photometrically anomalous area is very sharp (abrupt reflectance dropoff), (b) the shape of the area has no preferential pattern and (c) in some instances it can follow the boulder outline in planar view, (d) the size of the area increases with increasing size of the hosting boulder, and (e) ranges from one third to the almost complete boulder area in planar view.

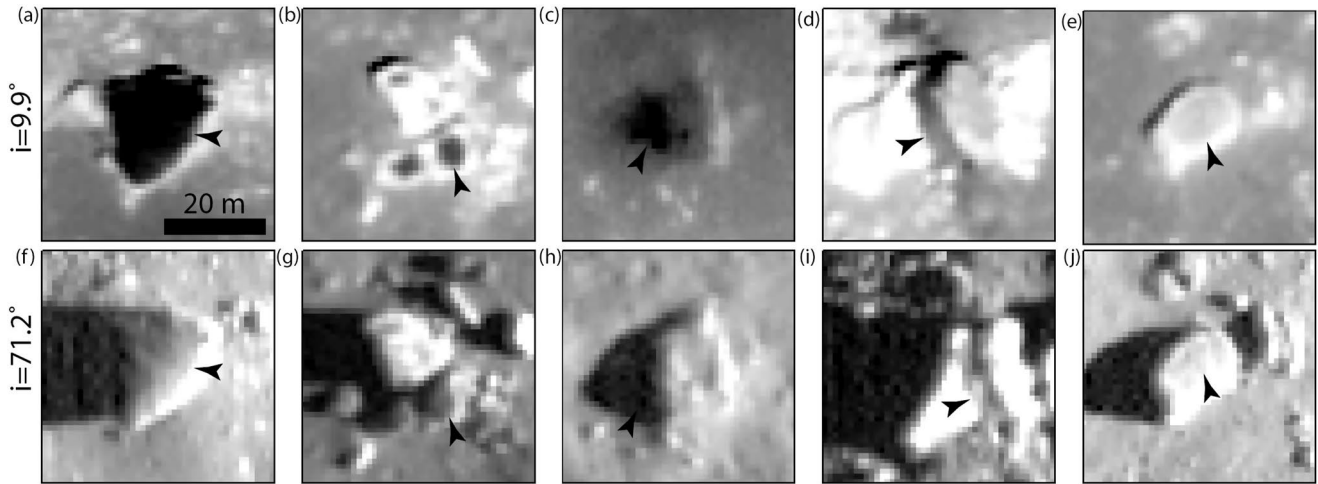


**Figure 2.** Photometrically anomalous dusty boulders (a–d and f–i) and a normal dusty boulder (e, j), shown twice at low (upper row) and high (lower row) incidence angle. Arrows point to the dust mantling. Reflectance value 0.06–0.11 in upper row and 0.0–0.03 in lower row. Panel (b) is the only detection in the catalog of Rüsich and Bickel (2023). Location numbers in Figure 1 are (a, f) location 4; (b, g) location 3; (c, h) location 2; (d, j) location 25. LROC NAC images M1285164183 and M1200481033. Scale bar in (a) applies to all panels.

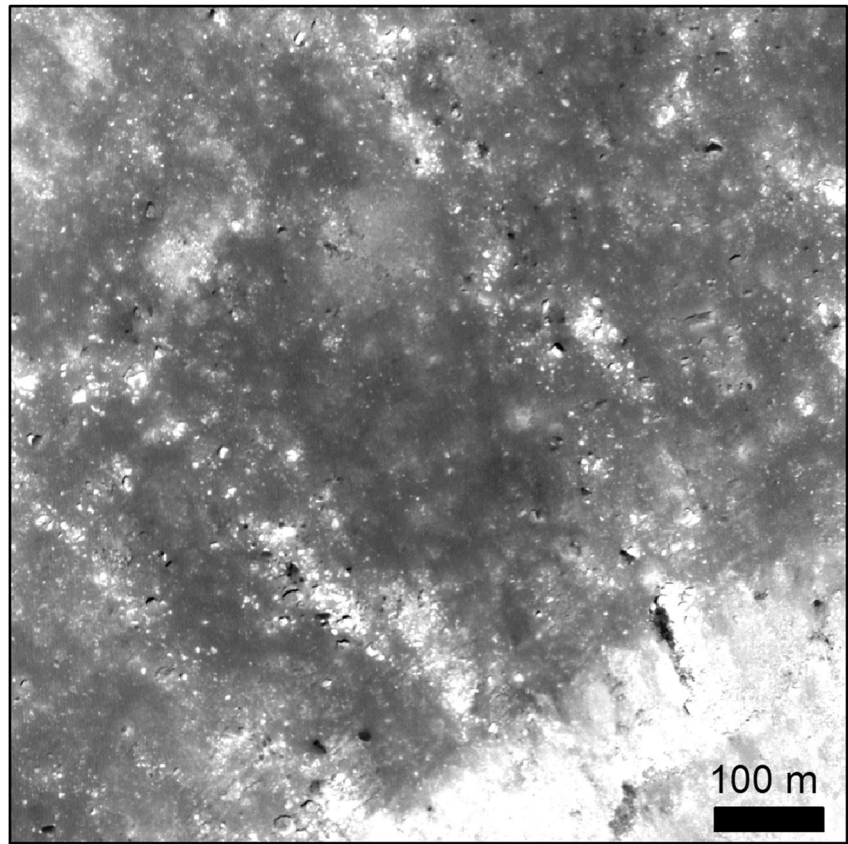


**Figure 3.** The northwestern area of the rim of Reiner K crater was imaged with an incidence angle of  $9.9^\circ$  and displayed with a 0.06–0.11 reflectance range (image M1285164183). The darkest features represent the photometrically anomalous dusty boulders (PADBs). Note trains of bright boulders radial to the crater rim (lower right). The spatial distribution of PADBs follows that of brighter non-PADBs.

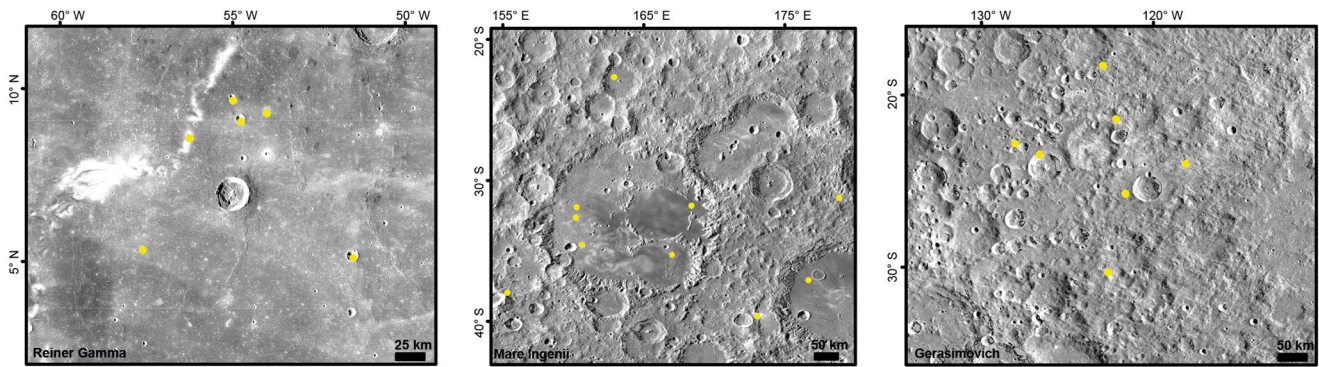


**Figure 4.** Three regions where the search for additional photometrically anomalous dusty boulders was performed. The regions correspond to the swirls of Reiner Gamma (left), Mare Ingenii (center) and Gerasimovich (right). Yellow dots indicate the location of impact craters that host boulders with size larger than a few meters.

The small photometrically anomalous areas are only a few pixels wide and thus too small to clearly identify their shape and association with other boulders: They are not considered further in the analysis.

For large PADBs, the association between the photometrically anomalous area and the hosting boulder can be grouped into two types depending on the position of the area relative to the boulder: “on top” or “on the side.” There are few instances of intermediate morphology suggesting that a continuum exists between the two end-members. The “on top” type is characterized by areas most often at the center of large (~10–20 m) boulders with sharp boundaries to the surrounding rock surface (Figures 2a–2f and 2b, 2g). Nearby boulders of the same size and similar reflectance can lack the photometrically anomalous area. In this type, we observe one instance (Figures 2b and 2g) with an impact fragmentation morphology resulting from the fragmentation of a parent boulder into several large fragments (e.g., Durda, 2023; Ruesch et al., 2020). Noteworthy, few of the fragments have their own photometric anomalous area on top. Even if the rock material of the fragments is the same (common parent boulder), the area extent is not shared between the fragments but is split into distinct features. It is reasonable to assume that the parent boulder of the fragments in Figures 2b and 2g had an anomalous dust area as well. Therefore, this example suggests that the property generating the anomalous dust is preserved even after a rock is split. The “side” type is characterized by a photometrically anomalous area extending from the center or flank of the hosting boulder until the background terrain, and not by a spatial extent limited to the boulder center (Figures 2c, 2h and 2d, 2i). There is no clear indication that areas extend onto the nearby regolith because shadows often obscure part of the scene and the boundary of the boulder cannot be seen everywhere. However, we cannot exclude the possibility that areas reach the adjacent regolith and get spatially mixed with it (Figure 2c). In any case, large photometrically anomalous areas lying only on regolith ground without being juxtaposed to a boulder are not present (whether this occurs for smaller areas is uncertain because of the limited resolution).

On the southeastern crater wall of Reiner K, mass wasting and outcrop material display similarly low reflectances at low incidence angles. Here, the material presents a diffuse boundary downslope. This site is in shadow at high incidence angle images and can therefore not be studied in detail. For completeness, we note that a rille and a flat-floored depression of volcanic origin, typical of mare units (e.g., Wilhelms et al., 1987), are located a few kilometers away from the crater rim in the southern and eastern directions, respectively (Figure 1).

At and near the investigated swirls, including Reiner Gamma, there are only a few craters meeting the search criteria: 6 craters for Reiner Gamma, 10 for Mare Ingenii, 7 for Gerasimovich (Figure 4). In none of these additional craters, PADBs were identified.

### 3.2. Photometry

To further quantify the photometric behavior, the Hapke model was inverted to obtain the parameters  $w$ ,  $b_h$ ,  $c_h$ , and  $B_{50}$  for one feature type and the inclination angle ( $\Theta$ ) for each of the six locations for one feature type. The selected locations around the crater Reiner K are displayed in Figure 1 and color-coded for the different feature types. The selected features were chosen to have image information from all available phase angle images and to not lie in the shadow in one of the images. This ruled out some PADB locations in the western area, which are not covered by all images, and the crater slopes, which are shadowed in the large phase angle images. The estimated

**Table 2**  
*Estimated Inclination Angles for All Locations for the Four Feature Types*

Feature type	Location	Inclination mean [deg]	Inclination Stddev [deg]
PADB	1	-3.95	0.15
	2	-0.27	0.54
	3	29.93	4.37
	4	8.76	1.50
	5	4.00	1.01
	6	17.37	2.63
Bright Regolith	7	10.32	1.27
	8	1.27	0.49
	9	2.77	0.62
	10	12.40	1.44
	11	0.26	0.41
	12	13.90	1.58
Dark Regolith	13	7.83	0.89
	14	7.97	0.89
	15	-2.52	0.18
	16	7.09	0.86
	17	8.31	1.04
	18	-1.28	0.28
Normal Boulder	19	27.21	4.00
	20	12.96	2.32
	21	29.17	4.17
	22	22.60	3.39
	23	11.09	1.85
	24	33.52	3.98

*Note.* Means of the posterior distributions and uncertainties of the inclination angle in units of standard deviation in degrees.

mean inclination angles and their associated uncertainties are listed for all selected locations in Table 2. The uncertainties of the inclination angles are generally small but usually larger for the two boulder feature types relative to the non-boulder feature types.

In Figure 5, the locations selected for the PADB feature type from image M109589691 are displayed. The PADBs appear dark in the small phase angle image, and the pixels are selected in the center of these dark areas (marked in yellow). The Bayesian inference results for the PADBs are shown in Figure 6, and the corresponding means are listed in Table 3. Notably, the parameters of the phase function cannot be determined reliably. Acceptable solutions to the inversion are backscattering ( $c_h > 0$ ) but also forward scattering ( $c_h < 0$ ). To effectively constrain the parameters of the phase function, even when they are coupled using the hockey stick relation, data for phase angles larger than  $90^\circ$ , or at least between  $20$  and  $70^\circ$  are required to gain information about the shape of the phase curve where the influence of the opposition effect is comparatively small. As no NAC observations are available for such phase angles, all solutions in this broad range can be seen as acceptable. To sample the entire space of suitable solutions, however, it is reasonable to keep the parameters in the model as long as the other parameters can still be determined reliably, as is the case here because several observations at similar phase angles are available. The PADB albedo is small but similar to the albedo of the normal regolith background pixels (see Table 3). The posterior distribution of  $B_{50}$  shows that the values are almost normally distributed around the mean 0.957 with a standard deviation of 0.222 and, accounting for the correlation with the albedo, the corrected value becomes 0.565.

The bright regolith and dark regolith locations were selected in the proximity of the PADB locations to investigate whether the regolith and the dust emplaced on the boulders show similar photometric behavior (Figure 5). The resulting posterior distributions of the Hapke parameters are shown in Figures 7 and 8 for dark and bright regolith, respectively. The albedo of bright regolith (mean 0.272) is larger compared to the values of the PADB and dark regolith. The opposition effect is more pronounced for the background regolith locations with 1.202 and 1.446 for the bright and dark regolith, respectively. As expected, according to the general correlation between albedo and opposition effect strength by Sato et al. (2014), the opposition effect is stronger for the darker regolith compared to the bright regolith.

When the correlation is accounted for and the corrected values are calculated, the regolith pixels, bright or dark, show slightly reduced opposition effect strength compared to the average lunar regolith (see Table 3), that is, the values are below one. However, these regolith values are still higher compared to those of the PADB feature type. The posterior distribution of the phase function parameters again covers the entire range and cannot be constrained with the available data.

Overall, the uncertainties for the normal boulder feature type are larger compared to the other feature types. In part, this uncertainty stems from the more uncertain inclination angle determination, and the overall fit is worse, as can be seen in the likelihood function standard deviation, which is higher compared to the other feature types. This can also be attributed to stronger photometric variations within the selected locations. The boulders represent the highest albedo material with 0.353 (Figure 9). However, even though the albedo is very high, the opposition effect strength is still higher compared to the PADB feature type, contrary to the typical trend observed on the Moon. Figure 10 shows the distribution of the  $B_{50,c}$  parameter for all feature types. For each sample in the Markov Chain Monte Carlo simulation, the value of  $B_{50,c}$  is calculated based on the albedo and  $B_{50}$  of that specific sample.

The mean values listed in Table 3 show that the smallest value corresponds to the PADB feature type. This confirms the finding that the dark areas appear only comparatively dark in the small phase angle images, but the contrast gets diminished in the large phase angle (and large incidence angle) images. The photometrical differ-



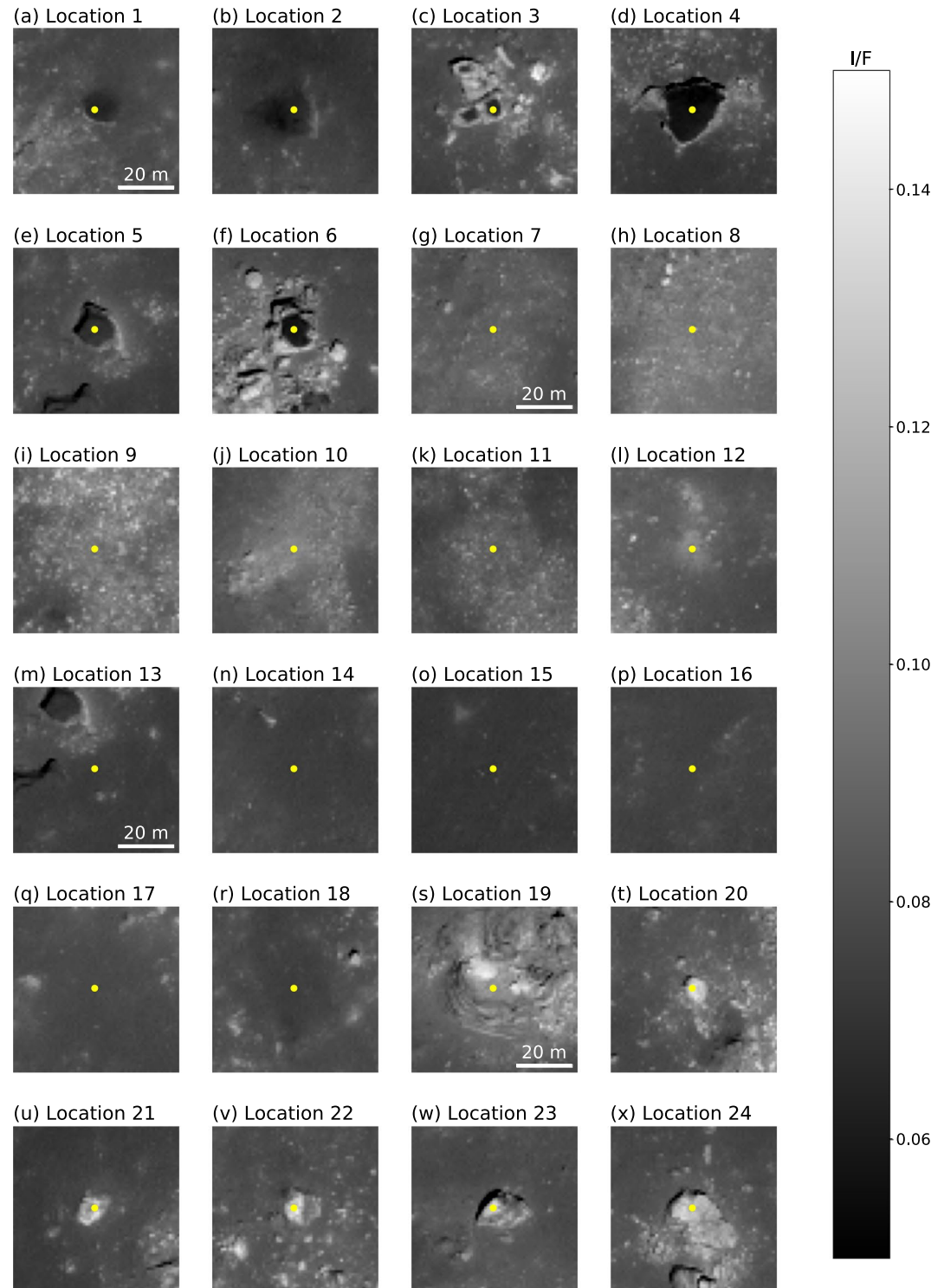


**Figure 5.** The pixels selected for the photometric modeling are marked in yellow in the reference image M109589691RE/LE. Locations 1–6 in subfigures a–f represent the PADB feature type. Locations 7–12 in subfigures g–l represent the bright regolith feature type. Locations 13–18 in subfigures m–r represent the dark regolith feature type. Locations 19–24 in subfigures s–x represent the normal boulder feature type.

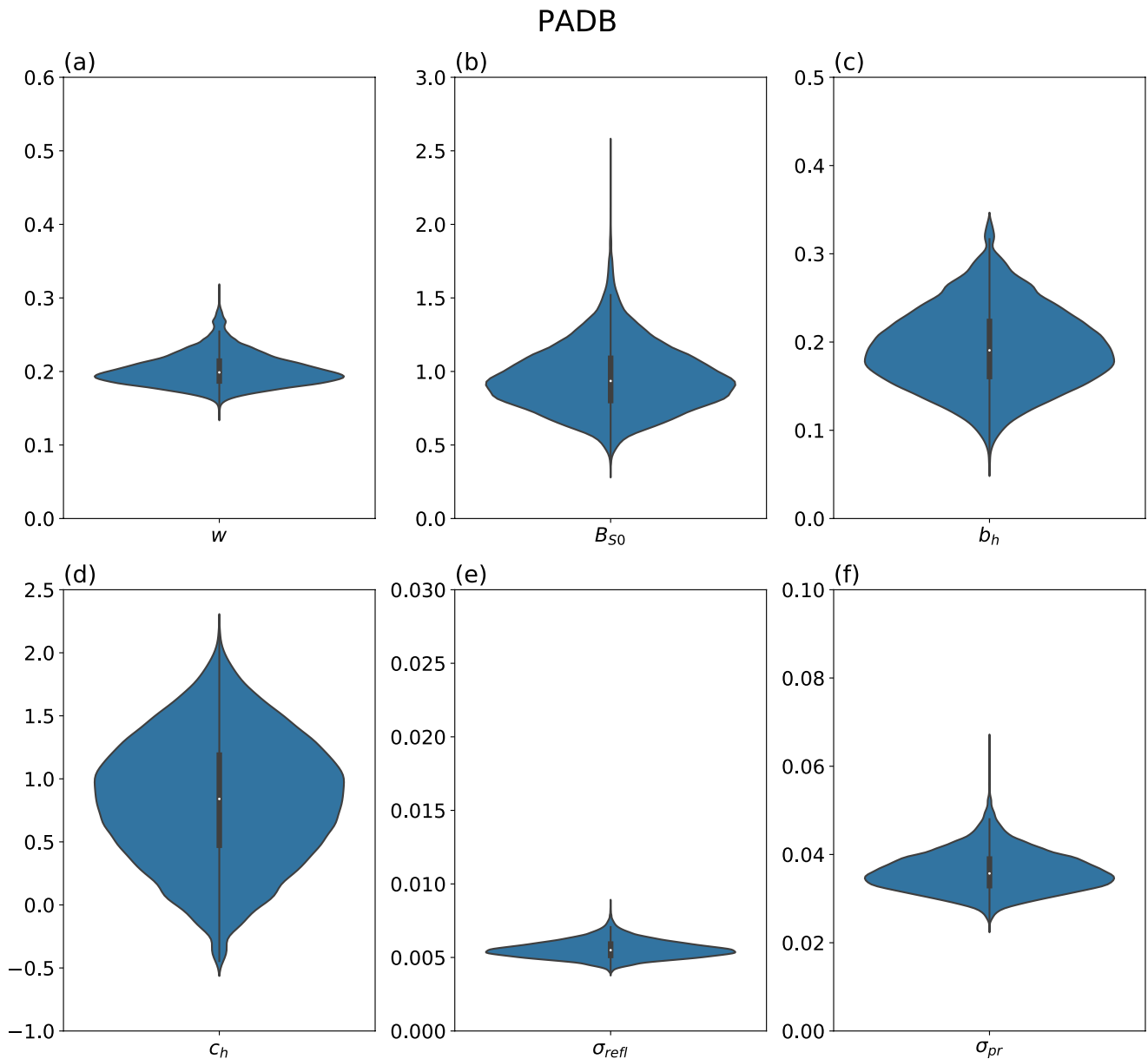


Figure 6. Posterior distributions of photometric and Bayesian model parameters, given the data for the locations (1–6) representing the PADB feature type.

Table 3  
Estimated Mean Parameters for All Four Feature Types

Mean	$w$	$b_h$	$c_h$	$B_{50}$	$B_{50,c}$	$\sigma_{refl}$	$\sigma_{pr}$
PADB	0.202	0.193	0.829	0.957	0.565	0.0056	0.036
Bright Regolith	0.272	0.201	0.735	1.202	0.743	0.0056	0.025
Dark Regolith	0.199	0.195	0.799	1.446	0.854	0.0027	0.022
Normal Boulder	0.353	0.213	0.618	1.031	0.657	0.0084	0.037

Note.  $B_{50,c}$  denotes the corrected  $B_{50}$  with the influence of the albedo removed.

ence between the PADB locations and the dark regolith feature type is mainly due to differences in opposition effect strength and not because of albedo differences as it would appear from small phase angle images alone. The opposition effect is excessively small for the PADB dark area even compared to normal boulders.

#### 4. Discussion

Here we explain how the results of this study suggest that (i) PADB are not the direct result of a known impact crater process-like impact melt deposition (ii) PADBs are intrinsically related to the material composing some, but not all, boulders, and (iii) the material composing the PADB boulders differs from that of non-PADB in terms of still unclear properties.

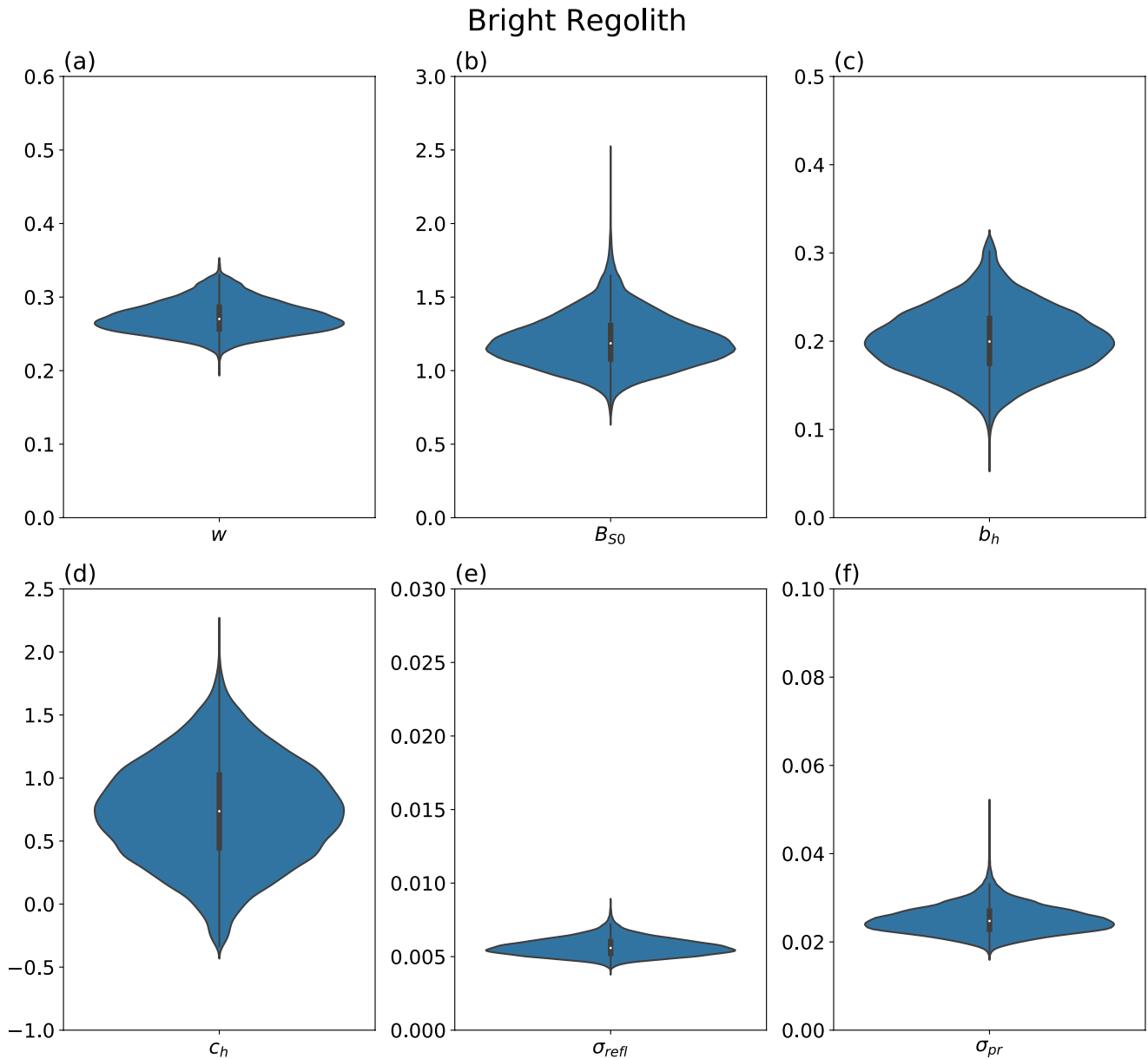


**Figure 7.** Posterior distributions of photometric and Bayesian model parameters, given the data for the locations (7–12) representing the bright regolith feature type.

#### 4.1. Incompatibility With Direct Formation by Ejecta Processes

Since the dark areas are located on crater ejecta, and ejecta emplacement is known to involve several complex mechanisms (e.g., Kenkmann et al., 2018; Melosh, 1989), one might expect that the formation of these features occurred as part of the ejecta emplacement process. However, their unique association with boulders argues against a formation as impact melt veneer (e.g., Bray et al., 2010; Denevi et al., 2012; Plescia & Spudis, 2014). Instead, since their morphological characteristics are identical to classical dust on boulders and they differ only in terms of the photometric behavior at a low incidence angle, the areas are likely to correspond to a dust coverage. It is evident that because the areas occur only on boulders while not all boulders host them, the process responsible for their formation is likely highly dependent on the boulder material, and thus not directly related to the ejecta emplacement process. Therefore, processes that photometrically affect ubiquitously large areas of an ejecta blanket, such as high-velocity jetted vapor (e.g., Speyerer et al., 2016) or impact shock (and associated melt) into boulders at the time of their excavation (Marshall et al., 2023), can be excluded. Vapor jetted soils (e.g.,

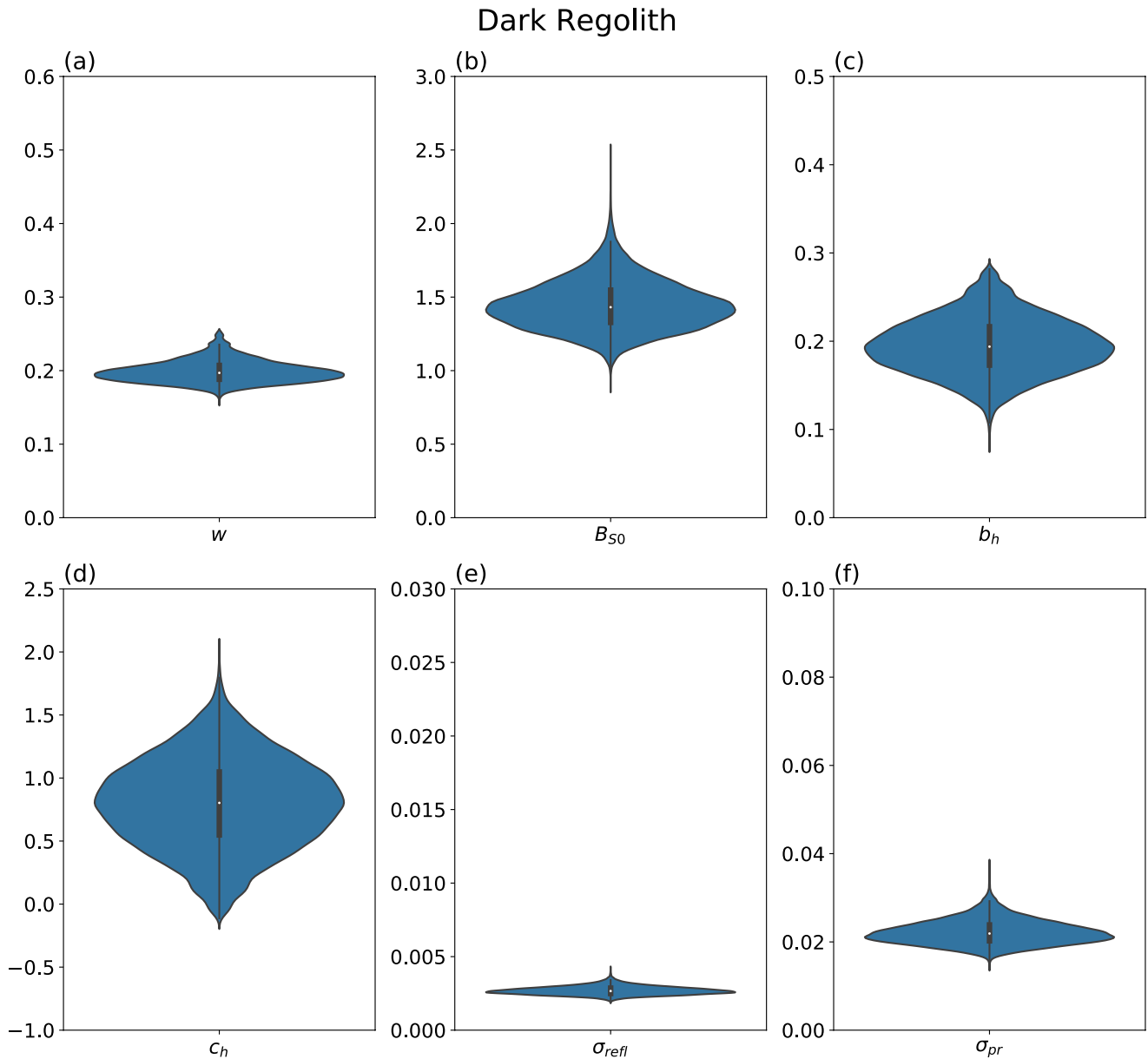


**Figure 8.** Posterior distributions of photometric and Bayesian model parameters, given the data for the locations (13–18) representing the dark regolith feature type.

Robinson et al., 2015; Speyerer et al., 2016) and impact shocked boulder fields (e.g., Marshal et al., 2023) can have an asymmetric distribution around the impact crater and do not display a spatial heterogeneity at the scale of single boulders. Another argument indicating an origin not directly related to the ejecta is the potential presence of photometrically anomalous dust on the inner wall of Reiner K near outcrops. However, as mentioned earlier, photometric data at a large phase angle for this area of the crater wall is incomplete and a clear identification as photometrically anomalous is not possible, that is, an effect based on albedo alone cannot be disregarded.

#### 4.2. Role of the Material Composing the Boulders

The northwestern concentration and alignment of boulders is typical for the deposition of a block-rich ejecta filament (e.g., Krishna & Kumar, 2016) and reflects a proximity in the target material, for example, from a common compositional unit, before the impact (e.g., Kadono et al., 2019). This pattern in the northwest thus implies that the dark areas are on boulders that are compositionally similar or identical to each other, again suggesting that the

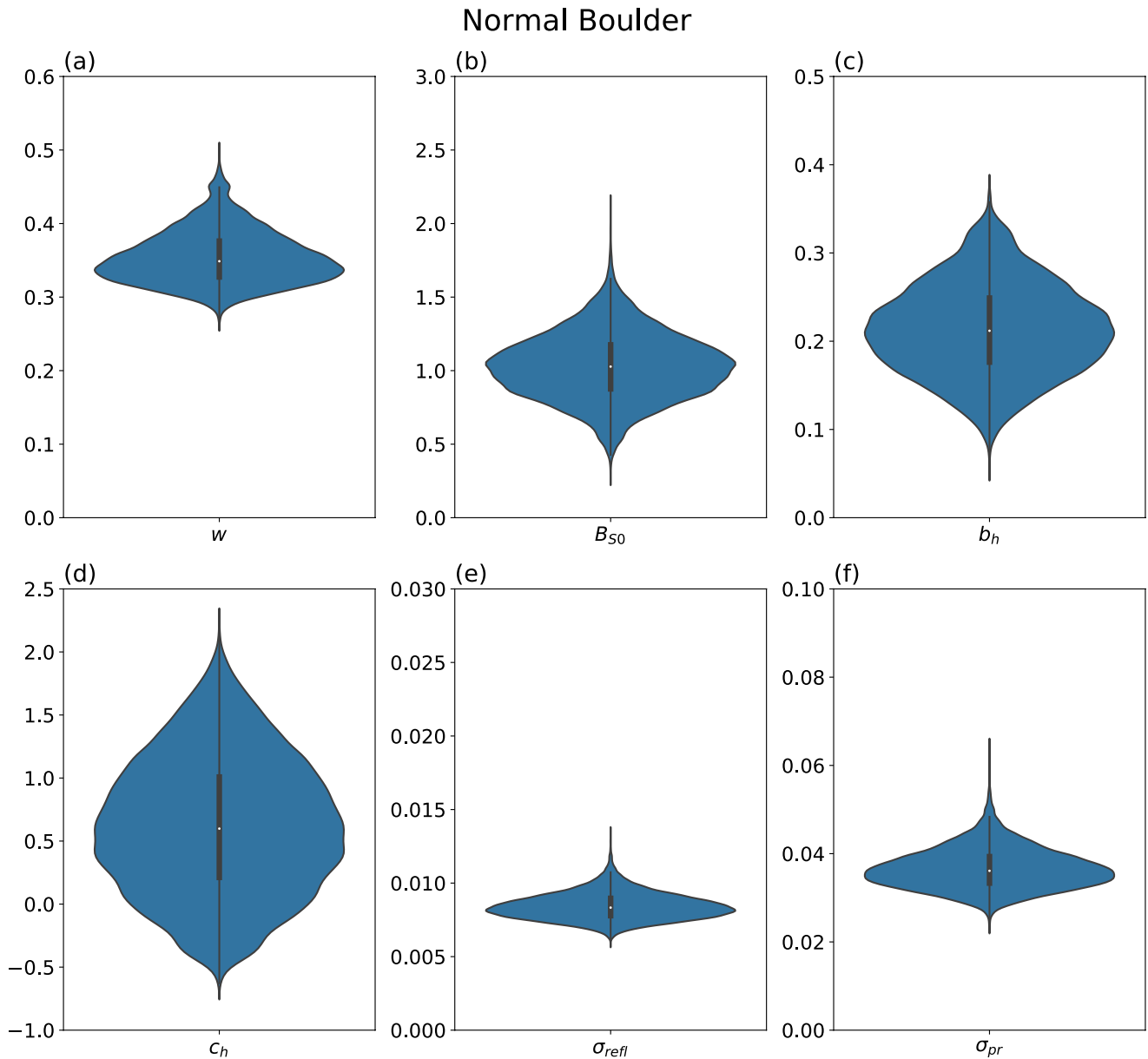


**Figure 9.** Posterior distributions of photometric and Bayesian model parameters, given the data for the locations 19–24 representing the normal boulder feature type without any dark areas.

material composing the boulder plays a key role. In other words, the peculiarity of the boulders is related to the peculiarity of the target from which these ejecta blocks were excavated. We thus seek a process able to affect the layer of dust particles on some, but not all, boulders such that the opposition effect is reduced while an albedo similar to a dark background regolith is maintained.

### 4.3. Chemical and Roughness Properties

Let us first consider two scenarios based on the difference in terms of chemistry and surface roughness between PADBs and non-PADBs. The first scenario foresees the development of a particular dust deposit due to thermal fatigue. It is known that boulders subjected to diurnal temperature variations develop thermal stresses (Molaro et al., 2017) and if composed of regolith breccia can develop micro-flakes (Patzek & Rüsçh, 2022). The formation and accumulation of micro-fragments could lead to the development of a boulder surface with unique properties, such as a surface preferentially covered by micro-flakes with a particular size and packing density. This

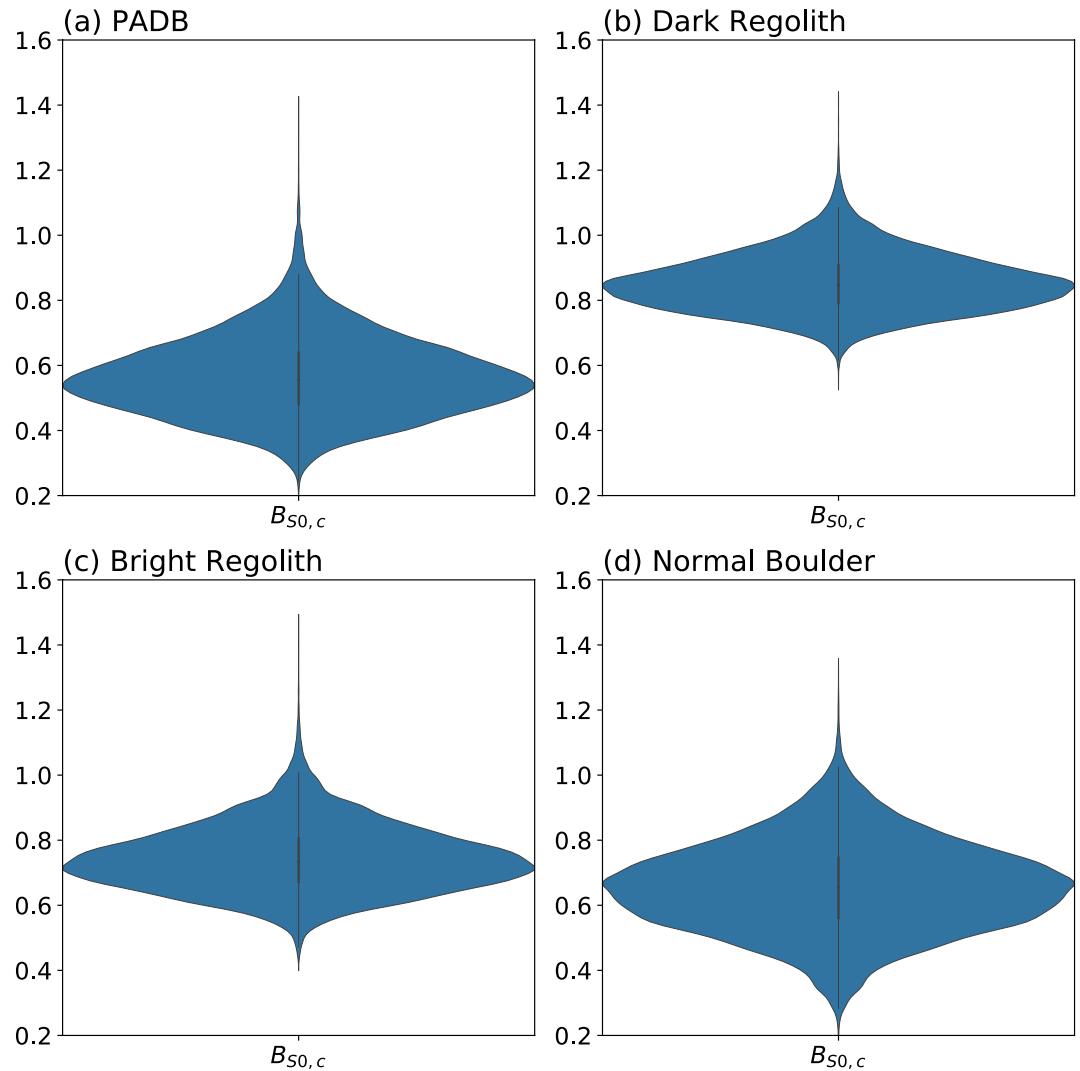


**Figure 10.** Posterior distributions of the  $B_{S0}$  corrected for the influence of the estimated albedo. Each sample in the chain is converted to  $B_{S0,c}$  using the albedo of that specific sample.

surface could in principle display particular photometric properties. This scenario bears some resemblances to one evoked for dust ponds around boulders on asteroid 433 Eros (Dombard et al., 2010) and in fact some PADB properties (i.e., dust deposit with sharp boundary with adjacent areas) are reminiscent of ponds. For lunar boulders, production of micro-flaking by thermal fatigue occurs for plagioclase and glass-rich petrologies like regolith breccia (Patzek & Rüsçh, 2022). These types of boulders are present throughout the Moon, in particular in the highlands, and thus cannot explain the observation of a highly localized occurrence. Another scenario considers the possibility that a peculiar composition and roughness lead to differences in photoelectron yield and local electric field (e.g., Dove et al., 2018; Feuerbacher et al., 1972; Xu et al., 2020) and thus variation in the dust charging and lofting. These variations could be particularly important at topographic reliefs (e.g., boulders) due to the formation of illuminated and shadowed regions (e.g., Berg, 1978; Farrell et al., 2007; Lee, 1996; Piquette & Horanyi, 2017; Poppe et al., 2012). On boulders, differences in lofting could develop dust soil of different properties, for example, packing densities, and thus different photometric properties. Future studies should consider which specific differences in composition and/or roughness between PADBs and non-PADBs would be required. In this scenario, it remains unclear why these properties are so unique that they are not observed elsewhere on the Moon.

#### 4.4. Magnetic Properties

We now turn to the peculiarities of the Reiner K crater and its location. It is a simple crater of 3 km diameter, and its ejecta boulders have been excavated from a depth of about 600 m, reasonably assuming a simple crater excavation mode (Melosh, 1989). The impact occurred about 70 km away from the magnetic anomaly of Reiner Gamma, where a magnetic flux density of  $>100$  nT at the surface level has been derived from orbital measurements (e.g., Tsunakawa et al., 2015). The source of the magnetic field is potentially a magnetized body, for example, a melt sheet of impact ejecta from a large basin that incorporated highly magnetic projectile material (e.g., Wieczorek et al., 2012). Several estimates of the properties of this body have been made. Overall, models approximate the shape of the body as an ellipsoid several tens of kilometers in width, located within a few kilometers below the surface, with a magnetization in the range of 1–100 A/m (e.g., Garrick-Bethell & Kelley, 2019; Hemingway & Garrick-Bethell, 2012; Nicholas et al., 2007). It might be possible that the actual horizontal extent of this body is greater than these estimates, so that it reaches the location of the Reiner K crater, and that it is regionally located at a shallower depth. Alternatively, at the periphery of this body, similar but much smaller and shallower melt sheets could have formed, whose sizes are too small to be resolved by orbital measurements (e.g., Zimmerman et al., 2015). If this is the case, the Reiner K impact might have excavated material from a magnetized body associated with Reiner Gamma and brought up to the surface body fragments with magnetization in the form of ejecta boulders. Additional boulders would have been ejected by Reiner K from the non-magnetized section of the target, such as, for example, volcanic units superposing the magnetized body. The heterogeneity of the target (e.g., Figure 13 in Mustard et al., 2011) would thus explain the spatial distribution of PADB and non-PADB. It is unlikely that dust grains containing submicroscopic iron particles (e.g., Oder, 1991; Taylor et al., 2005) could be attracted directly by a boulder's magnetic force, and thus, preferential dust movement/deposition occurs. In fact, considering a typical weight fraction of  $\text{Fe}^0$  in dust grains of  $\sim 1$  wt.%, the gradient of the magnetic flux density of putative magnetic boulders would need to be very high (0.1–1 T/m) for the attraction to be of the same order of magnitude or even higher than the Moon's surface gravity. However, it might be conceivable that the magnetic field plays an indirect role. For example, the charge separation by a magnetic field causes electric fields that in turn influence the motion of dust (e.g., Garrick-Bethell et al., 2011) and therefore modify or prevent the formation of normal soil structure, leading to an anomalous photometry. Additionally, lofted dust dynamics and soil development indirectly influenced by a magnetic field have been experimentally performed by Yeo et al. (2022). That study shows that while the magnetic field does not directly influence the dust motion, it controls the movement of electrons, creating regions of active and inactive lofting. However, while the physical parameters in the Yeo et al. (2022) laboratory experiment (e.g., the magnetic flux density) are chosen to scale with a lunar magnetic anomaly, they are not fully representative, in particular concerning the strength of the magnetic field relative to the near-surface electric field. The hypotheses related to electric fields formed by charge separation above a magnetized PADB or active and inactive regions of lofting at a magnetized PADB, have been proposed previously on a spatial scale of kilometers. We thus encourage further modeling studies to investigate these effects on the spatial scale of individual boulders. These latter scenarios assume a prolonged and continuous soil modification and anomalous soil development. An additional scenario considers the formation of the anomalous features to be restricted to the final phases of crater development. During impact and crater development, transient magnetic fields develop, whose strength can be a few orders of magnitude higher than during post-crater development (e.g., Cisowski et al., 1977; Crawford, 2020). Such conditions, coupled with the potential preexisting magnetic properties of some of the exposed material, might have been favorable for the formation of the observed abnormal dust soil. It remains unclear why no additional PADB were observed elsewhere near or in other swirls. Possibly, the reason lies in the rarity of the appropriate conditions for the development of PADB. In fact, near swirls fresh and sufficiently large craters are rare, and within swirls, it is likely that the anomalous photometric behavior does not occur exactly as outside the swirl because of their peculiar surficial conditions (e.g., Blewett et al., 2011; Hess et al., 2020; Hood & Schubert, 1980; Kaydash et al., 2009; Kreslavsky & Shkuratov, 2003; Pinet et al., 2000).

#### 5. Conclusion

We investigated boulders with peculiar features visible in optical images acquired by the LRO NAC camera. The boulders likely are ejecta blocks from the crater Reiner K, and the features represent a dust mantling covering the top and/or sides of the boulders. The dust mantling has an uncommon photometric behavior that leads to a particularly dark appearance in images acquired at low incidence angles. This photometric behavior is only

present in some but not all dust-covered boulders around Reiner K. Apart from the anomalous photometrical behavior, these dust-covered boulders show no further difference with respect to other boulders. The photometric anomaly is most likely due to a reduced opposition effect associated with a more compact dust structure different from the normal regolith. A number of processes presented in the literature and their combination can be invoked to explain the multitude of observational constraints. Such processes involve dust and soil dynamics influenced by local topography, rock microstructure, rock chemical properties, as well as electrostatic levitation and magnetic fields. It is nevertheless unclear how such a potential interplay may work, and therefore the details of the mechanism responsible for the anomalies remain elusive. The spatial proximity to Reiner Gamma suggests that similar processes and/or similar anomalous properties might occur at both locations. We suggest that the Lunar Vertex mission (Blewett et al., 2022) should pay particular attention to the photometric behavior of dust on and near boulders and smaller rocks, as some of these might modify the canonical regolith structure and the associated photometrical behavior.

## Appendix A

### A1. Prior Distributions

In Bayesian inference, prior knowledge about the likely distribution of parameters can be incorporated with the so-called prior distributions. For each parameter of the model, a distribution can be defined, which together with the likelihood function constitutes the posterior density.

The albedo ( $w$ ) is physically only plausible in the interval between zero and one, but we do not include any further prior knowledge so that the prior is equally distributed in that interval:

$$p(w) \sim \text{Beta}(w \mid \alpha = 1, \beta = 1) \quad (\text{A1})$$

The phase function parameter  $b_h$  on the Moon has, according to Sato et al. (2014), an average approximate value of 0.24 in the visible range and, according to Warell (2004), a global average value of 0.21. It is also limited to the interval  $[0, 1]$  so that a Beta distribution is suitable. We set the mean to approximately 0.225 so that the prior becomes

$$p(b_h) \sim \text{Beta}(b_h \mid \alpha = 10, \beta = 34.85) \quad (\text{A2})$$

The shadow hiding opposition effect amplitude prior is given by a lognormal distribution with a mode at approximately 1.5 according to:

$$p(B_{S0}) \sim \text{LogNormal}(B_{S0} \mid \mu = 0.4, \sigma = 1) \quad (\text{A3})$$

We selected pixel locations of relatively flat pixels at the visible resolution. Therefore, we assumed that the inclination angle is equally likely between  $\pm 40^\circ$  tilt when compared to a flat surface.

$$p(\Theta) \sim \prod_{i=1}^N \text{Beta}\left(\frac{\Theta + 40}{80} \mid \alpha = 1, \beta = 1\right) \quad (\text{A4})$$

For the Bayesian model, the standard deviation of the likelihood function is commonly set to a half - normal distribution. Consequently, we define

$$p(\sigma_{\text{ref1}}) \sim \text{HalfNormal}(\sigma_{\text{ref1}} \mid \sigma = 1), \quad (\text{A5})$$

and

$$p(\sigma_{\text{phase}}) \sim \text{HalfNormal}(\sigma_{\text{phase}} \mid \sigma = 1) \quad (\text{A6})$$

for the reflectance and phase ratio parts of the model, respectively.



## Data Availability Statement

The LROC NAC data used in this study are available at the NASA Planetary Data System (Robinson, 2009). Derived data of this study, that is, the posterior distributions of photometric and Bayesian model parameters, are available under <https://doi.org/10.60520/IEDA/113071> (Rüsch et al., 2023). This article made use of a catalog of images of lunar fractured boulders freely available from BORIS, the Bern Open Repository and Information System (Bickel, 2023).

## Acknowledgments

The constructive comments by two anonymous reviewers are acknowledged. OR, RMM and MP are supported by a Sofja Kovalevskaja Award of the Alexander von Humboldt foundation. HH is supported by a DIAS Research Fellowship in Astrophysics. HH gratefully acknowledges financial support from Khalifa University's Space and Planetary Science Center (Abu Dhabi, UAE) under Grant KU-SPSC- 8474000336. Open Access funding enabled and organized by Projekt DEAL.

## References

- Bandfield, J. L., Ghent, R. R., Vasavada, A. R., Paige, D. A., Lawrence, S. J., & Robinson, M. S. (2011). Lunar surface rock abundance and regolith fines temperatures derived from LRO Diviner Radiometer data. *Journal of Geophysical Research*, *116*(E12), E00H02. <https://doi.org/10.1029/2011Je003866>
- Berg, O. E. (1978). Alunar terminator configuration. *Earth and Planetary Science Letters*, *39*(3), 377–381. [https://doi.org/10.1016/0012-821x\(78\)90025-0](https://doi.org/10.1016/0012-821x(78)90025-0)
- Bickel, V. T. (2023). Dataset of: Global mapping of fragmented rocks on the Moon with a neural network: Implications for the failure mode of rocks on airless surfaces [Dataset]. Bern Open Repository and Information System (BORIS). <https://doi.org/10.48620/224>
- Bishop, C. M., & Nasrabadi, N. M. (2006). *Pattern recognition and machine learning*. Springer.
- Blewett, D. T., Coman, E. I., Hawke, B. R., Gillis-Davis, J. J., Purucker, M. E., & Hughes, C. G. (2011). Lunar swirls: Examining crustal magnetic anomalies and space weathering trends. *Journal of Geophysical Research*, *116*(E2), E02002. <https://doi.org/10.1029/2010JE003656>
- Blewett, D. T., Halekas, J., Ho, G. C., Greenhagen, B. T., Anderson, B. J., Vines, S. K., et al. (2022). Lunar Vertex: PRISM exploration of Reiner Gamma. In *Lunar and Planetary Science Conference*. abstract nr. 1131.
- Bray, V. J., Tornabene, L. L., Keszthelyi, L. P., McEwen, A. S., Hawke, B. R., Giguere, T. A., et al. (2010). New insight into lunar impact melt mobility from the LRO camera. *Journal of Geophysical Research*, *37*(21). <https://doi.org/10.1029/2010GL044666>
- Cisowski, S. M., Collinson, D. W., Runcorn, S. K., Stephenson, A., & Fuller, M. (1983). A review of lunar paleointensity data and implications for the origin of lunar magnetism. In *Lunar and Planetary Science Conference* (Vol. 88, pp. A691–A704).
- Cisowski, S. M., Fuller, M., & Hale, C. (1977). On the intensity of ancient lunar magnetic fields. In *Lunar and Planetary Science Conference* (Vol. 8, pp. 187–189).
- Crawford, D. A. (2020). Simulations of magnetic fields produced by asteroid impact: Possible implications for planetary paleomagnetism. *International Journal of Impact Engineering*, *137*, 103464. <https://doi.org/10.1016/j.ijimpeng.2019.103464>
- Denevi, B. W., Koeber, S. D., Robinson, M. S., Garry, W. B., Hawke, B. R., Tran, T. N., et al. (2012). Physical constraints on impact melt properties from Lunar Reconnaissance. *Icarus*, *219*(2), 665–675. <https://doi.org/10.1016/j.icarus.2012.03.020>
- Denevi, B. W., Robinson, M. S., Boyd, A. K., Blewett, D. T., & Klima, R. L. (2016). The distribution and extent of lunar swirls. *Icarus*, *273*, 53–67. <https://doi.org/10.1016/j.icarus.2016.01.017>
- Dombard, A. J., Barnouin, O. S., Prockter, L. M., & Thomas, P. C. (2010). Boulders and ponds on the Asteroid 433 Eros. *Icarus*, *210*(2), 713–721. <https://doi.org/10.1016/j.icarus.2010.07.006>
- Dove, A., Horányi, M., Robertson, S., & Wang, X. (2018). Laboratory investigation of the effect of surface roughness on photoemission from surfaces in space. *Planetary and Space Science*, *156*, 92–95. <https://doi.org/10.1016/j.pss.2017.10.014>
- Durda, D. D. (2023). Impact experiments into Bennu- and Ryugu-like regolith simulants I: Boulder fracture progression. In *Lunar and Planetary Science Conference*. abstract nr. 1170.
- Dutro, J. T. J., Dietrich, R. V., & Foose, R. M. (1989). *AGI data sheets: For geology in the field, laboratory, and office* (3rd ed.). American Geological Institute.
- Farrell, W. M., Stubbs, T. J., Vondrak, R. R., Delory, G. T., & Halekas, J. S. (2007). Complex electric fields near the lunar terminator: The near-surface wake and accelerated dust. *Geophysical Research Letters*, *34*(14). <https://doi.org/10.1029/2007GL029312>
- Feuerbacher, B., Anderegg, M., Fitton, B., Laude, L. D., Willis, R. F., & Grard, R. J. L. (1972). Photoemission from lunar surface fines and the lunar photoelectron sheath. In *Lunar and Planetary Science Conference* (pp. 2655–2663).
- Florensky, K. P., Basilevsky, A. T., Zezin, R. B., Polosukhin, V. V., & Popova, Z. V. (1978). Geologic-morphologic studies of lunar surface. In *Movable Laboratory on the Moon—Lunokhod 1.V.2* (pp. 102–135). Nauka Press.
- Garrick-Bethell, I., Head, J. W., & Pieters, C. M. (2011). Spectral properties, magnetic fields, and dust transport at lunar swirls. *Icarus*, *212*(2), 480–492. <https://doi.org/10.1016/j.icarus.2010.11.036>
- Garrick-Bethell, I., & Kelley, M. R. (2019). Reiner Gamma: A magnetized Elliptical Disk on the Moon. *Geophysical Research Letters*, *46*(10), 5065–5074. <https://doi.org/10.1029/2019GL082427>
- Gelman, A., Vehtari, A., Carlin, J. B., Stern, H. S., & Rubin, D. B. (1995). *Bayesian data analysis*. Chapman and Hall/CRC.
- Hapke, B. (2002). Bidirectional reflectance spectroscopy: 5. The coherent backscatter opposition effect and anisotropic scattering. *Icarus*, *157*(2), 523–534. <https://doi.org/10.1006/icar.2002.6853>
- Hapke, B. (2012). *Theory of reflectance and emittance spectroscopy*. Cambridge university press.
- Hemingway, D., & Garrick-Bethell, I. (2012). Magnetic field direction and lunar swirl morphology: Insights from Airy and Reiner Gamma. *Journal of Geophysical Research*, *117*, E10. <https://doi.org/10.1029/2012JE004165>
- Hess, M., Wöhler, C., Bhatt, M., Berezhnoy, A. A., Grumpe, A., Wohlfarth, K., et al. (2020). Processes governing the VIS/NIR spectral reflectance behavior of lunar swirls. *Astronomy & Astrophysics*, *639*, A12. <https://doi.org/10.1051/0004-6361/201937299>
- Hess, M., Wöhler, C., Qiao, L., & Bhatt, M. (2023). Comparative photometric analysis of the Reiner Gamma swirl and Chang'e 5 landing site. *A&A*, *674*, A226. <https://doi.org/10.1051/0004-6361/202346098>
- Hoffman, M. D., & Gelman, A. (2014). The No-U-turn sampler: Adaptively setting path lengths in Hamiltonian Monte Carlo. *Journal of Machine Learning Research*, 1593–1623.
- Hood, L. L., & Schubert, G. (1980). Lunar magnetic anomalies and surface optical properties. *Science*, *208*(4439), 49–51. <https://doi.org/10.1126/science.208.4439.49>
- Hörz, F., & Cintala, M. (1997). Impact experiments related to the evolution of planetary regoliths. *Meteoritics & Planetary Science*, *32*(2), 179–209. <https://doi.org/10.1111/j.1945-5100.1997.tb01259.x>
- Hörz, F., Schneider, E., & Hill, R. E. (1974). Micrometeoroid abrasion of lunar rocks: A Monte Carlo simulation. In *5th Lunar Conference* (Vol. 3, pp. 2397–2412).

- Johnson, B. C., Bowling, T. J., & Melosh, H. J. (2014). Jetting during vertical impacts of spherical projectiles. *Icarus*, 238, 13–22. <https://doi.org/10.1016/j.icarus.2014.05.003>
- Kadono, K., Suetsugu, R., Arakawa, D., Kasagi, Y., Nagayama, S., Suzuki, A. I., & Hasegawa, S. (2019). Pattern of impact-induced ejecta from granular targets with large inclusions. *The Astrophysical Journal Letters*, 880(2), L30. <https://doi.org/10.3847/2041-8213/ab303f>
- Kaydash, V., Kreslavsky, M., Shkuratov, Y., Gerasimenko, S., Pinet, P., Josset, J. L., & BeauvivreFoingFoing, S. B. B. (2009). Photometric anomalies of the lunar surface studied with SMART-1 AMIE data. *Icarus*, 202(2), 393–413. <https://doi.org/10.1016/j.icarus.2009.03.018>
- Keller, L. P., Wentworth, S. J., & McKay, D. S. (1997). Space weathering effects on Apollo 17 Breccia 76015: Reflectance spectroscopy and microstructure. In *Lunar and Planetary Science Conference* (p. 1566).
- Kenkmann, T., Deutsch, A., Thoma, K., Ebert, M., Poelchau, M. H., Buhl, E., et al. (2018). Experimental impact cratering: A summary of the major results of the MEMIN research unit. *Meteoritics & Planetary Sciences*, 53(8), 1543–1568. <https://doi.org/10.1111/maps.13048>
- Kreslavsky, M. A., & Shkuratov, Y. G. (2003). Photometric anomalies of the lunar surface: Results from Clementine data. *Journal of Geophysical Research*, 108(E3), 5015. <https://doi.org/10.1029/2002JE001937>
- Krishna, P., & Kumar, P. S. (2016). Impact spallation processes on the Moon: A case study from the size and shape analysis of ejecta boulders and secondary craters of Censorinus crater. *Icarus*. <https://doi.org/10.1016/j.icarus.2015.09.033>
- Laura, J., Acosta, A., Addair, T., Adoram-Kershner, L., Alexander, J., Alexandrov, et al. (2022). Integrated software for Imagers and spectrometers (version 7.0.0). *Zenodo*. <https://doi.org/10.5281/zenodo.6558530>
- Lawrence, K., Johnson, C., Tauxe, L., & Gee, J. (2008). Lunar paleointensity measurements: Implications for lunar magnetic evolution. *Physics of the Earth and Planetary Interiors*, 168(1–2), 71–87. <https://doi.org/10.1016/j.pepi.2008.05.007>
- Lee, P., Veverka, J., Thomas, P. C., Helfenstein, P., Belton, M. J., Chapman, C. R., et al. (1996). Ejecta blocks on 243 Ida and on other asteroids. *Icarus*, 120, 1–105. <https://doi.org/10.1006/icar.1996.0039>
- Marshall, R. M., Rüschi, O., Wöhler, C., Wohlfarth, K., & Velichko, S. (2023). Photometry of LROC NAC resolved rock-rich regions on the Moon. *Icarus*, 394, 115419. <https://doi.org/10.1016/j.icarus.2022.115419>
- Melosh, H. J. (1989). Impact cratering a geological process. In *Oxford Monographs on Geology and Geophysics No. 11*. Oxford University Press.
- Molaro, J. L., Byrne, S., & Le, J.-L. (2017). Thermally induced stresses in boulders on airless body surfaces, and implications for rock breakdown. *Icarus*, 294, 247–261. <https://doi.org/10.1016/j.icarus.2017.03.008>
- Muehlberger, W. R., Batson, R. M., Boudette, E. L., Duke, C. M., Eggleton, R. E., Elson, D. P., et al. (1972). Preliminary geologic investigations of the Apollo 16 landing site. In *Apollo 16 Preliminary Science report*. NASA SP-315.
- Mustard, J. F., Pieters, C. M., Isaacson, P. J., Head, J. W., Besse, S., Clark, R. N., et al. (2011). Compositional diversity and geologic insights of the Aristarchus crater from the Moon Mineralogy Mapper data. *Journal of Geophysical Research*, 116, E00G12. <https://doi.org/10.1029/2010JE003726>
- Nicholas, J. B., Purucker, M. E., & Sabaka, T. J. (2007). Age spot or youthful marking: Origin of Reiner Gamma. *Geophysical Research Letters*, 34, 2. <https://doi.org/10.1029/2006GL027794>
- Oder, R. R. (1991). Magnetic separation of lunar soils. *IEEE Transactions on Magnetics*, 27(6), 5367–5370. <https://doi.org/10.1109/20.278841>
- Patzek, M., & Rüschi, O. (2022). Experimentally induced thermal fatigue on lunar and eucrite meteorites—Influence of the mineralogy on rock breakdown. *Journal of Geophysical Research: Planets*, 127(10), e2022JE007306. <https://doi.org/10.1029/2022JE007306>
- Pieters, C. M., & Noble, S. K. (2016). Space weathering on airless bodies. *Journal of Geophysical Research: Planets*, 121(10), 1865–1884. <https://doi.org/10.1002/2016JE005128>
- Pinet, P. C., Shevchenko, V. V., Chevrel, S. D., Daydou, Y., & Rosemberg, C. (2000). Local and regional lunar regolith characteristics at Reiner Gamma Formation: Optical and spectroscopic properties from Clementine and Earth-based data. *Journal of Geophysical Research*, 105(E4), 9457–9475. <https://doi.org/10.1029/1999je001086>
- Piquette, M., & Horányi, M. (2017). The effect of asymmetric surface topography on dust dynamics on airless bodies. *Icarus*, 291, 65–74. <https://doi.org/10.1016/j.icarus.2017.03.019>
- Plescia, J., & Spudis, P. D. (2014). Impact melt flows at Lowell crater. *Planetary and Space Science*, 103, 219–227. <https://doi.org/10.1016/j.pss.2014.08.003>
- Poppe, A. R., Piquette, M., Likhanskii, A., & Horányi, M. (2012). The effect of surface topography on the lunar photoelectron sheath and electrostatic dust transport. *Icarus*, 221(1), 135–146. <https://doi.org/10.1016/j.icarus.2012.07.018>
- Rennilson, J. J., & Criswell, D. R. (1973). Surveyor observations of lunar horizon-glow. *The Moon*, 10(2), 121–142. <https://doi.org/10.1007/BF00655715>
- Robinson, M. (2009). LRO MOON LROC 5 RDR V1.0, LRO-L-LROC-5-RDR-V1.0. *NASA Planetary Data System (PDS)*. <https://doi.org/10.17189/1520341>
- Robinson, M. S., Boyd, A. K., Denevi, B. W., Lawrence, S. J., McEwen, A. S., Moser, D. E., et al. (2015). New crater on the Moon and a swarm of secondaries. *Icarus*, 252, 229–235. <https://doi.org/10.1016/j.icarus.2015.01.019>
- Robinson, M. S., Brylow, S. M., Tschimmel, M., Humm, D., Lawrence, S. J., Thomas, P. C., et al. (2010). Lunar reconnaissance orbiter camera (LROC) instrument overview. *Space Science Reviews*, 150(1–4), 81–124. <https://doi.org/10.1007/s11214-010-9634-2>
- Ruesch, O., Sefton-Nash, E., Vago, J. L., Küppers, M., Pasckert, J. H., Khron, K., & Otto, K. (2020). In situ fragmentation of lunar blocks and implications for impacts and solar-induced thermal stresses. *Icarus*, 336, 113431. <https://doi.org/10.1016/j.icarus.2019.113431>
- Rüschi, O., & Bickel, V. T. (2023). Global mapping of fragmented rocks on the Moon with a neural network: Implications for the failure mode of rocks on airless surfaces. *Planetary and Space Science*, 4(7), 126. <https://doi.org/10.3847/PSJ/acd1ef>
- Rüschi, O., Hess, M., Wöhler, C., Bickel, V. T., Marshall, R. M., Patzek, M., & Huybrighs, H. L. F. (2023). Dataset for Discovery of a dust sorting process on boulders near the Reiner Gamma swirl on the Moon, Version 1.0. *Interdisciplinary Earth Data Alliance (IEDA)*. <https://doi.org/10.60520/IEDA/113071>
- Rüschi, O., Marshall, R. M., Iqbal, W., Pasckert, J. H., van der Bogert, C. H., & Patzek, M. (2022). Catastrophic rupture of lunar rocks: Implications for lunar rock size-frequency distributions. *Icarus*, 387, 115200. <https://doi.org/10.1016/j.icarus.2022.115200>
- Rüschi, O., & Wöhler, C. (2022). Degradation of rocks on the moon: Insights on abrasion from topographic diffusion, LRO/NAC and Apollo images. *Icarus*, 384, 115088. <https://doi.org/10.1016/j.icarus.2022.115088>
- Salvatier, J., Wiecki, T. V., Thomas, V., & Fonnesbeck, C. (2016). Probabilistic programming in Python using PyMC3. *PeerJ Computer Science*, 2, e55. <https://doi.org/10.7717/peerj-cs.55>
- Sato, H., Robinson, M. S., Hapke, B., Denevi, B. W., & Boyd, A. K. (2014). Resolved Hapke parameter maps of the Moon. *Journal of Geophysical Research: Planets*, 119(8), 1775–1805. <https://doi.org/10.1002/2013je004580>
- Schmidt, F., & Fernando, J. (2015). Realistic uncertainties on Hapke model parameters from photometric measurement. *Icarus*, 260, 73–93. <https://doi.org/10.1016/j.icarus.2015.07.002>

- Speyerer, E. J., Povilaitis, R. Z., Robinson, M. S., Thomas, P. C., & Wagner, R. V. (2016). Quantifying crater production and regolith overturn on the Moon with temporal imaging. *Nature*, *538*(7624), 215–218. <https://doi.org/10.1038/nature19829>
- Sun, L., & Lucey, P. G. (2022). Near-infrared spectroscopy of boulders with dust or patina coatings on the Moon: A two-layer radiative transfer model. *Icarus*, *387*, 115204. <https://doi.org/10.1016/j.icarus.2022.115204>
- Tarduno, J. A., Cottrell, R. D., Lawrence, K., Bono, R. K., Huang, W., Johnson, C. L., et al. (2021). Absence of a long-lived lunar paleomagnetosphere. *Science Advances*, *7*(32). <https://doi.org/10.1126/sciadv.abi7647>
- Taylor, L. A., Schmitt, H. H., Carrier, W. D., & Nakagawa, M. (2005). Lunar dust problem: From liability to asset. <https://doi.org/10.2514/6.2005-2510>
- Tikoo, S. M., Weiss, B. P., Shuster, D. L., Suavet, C., Wang, H., & Grove, T. L. (2017). A two-billion-year history for the lunar dynamo. *Science Advances*, *3*(8), e1700207. <https://doi.org/10.1126/sciadv.1700207>
- Tsunakawa, H., Takahashi, F., Shimizu, H., Shibuya, H., & Matsushima, M. (2015). Surface vector mapping of magnetic anomalies over the Moon using Kaguya and Lunar Prospector observations. *Journal of Geophysical Research: Planets*, *120*(6), 1160–1185. <https://doi.org/10.1002/2014je004785>
- Wang, X., Schwan, J., Hsu, H., Grün, E., & Horányi, M. (2016). Dust charging and transport on airless planetary bodies. *Geophysical Research Letters*, *43*(12), 6103–6110. <https://doi.org/10.1002/2016GL069491>
- Warell, J. (2004). Properties of the Hermean regolith: IV. Photometric parameters of Mercury and the Moon contrasted with Hapke modelling. *Icarus*, *167*(2), 271–286. <https://doi.org/10.1016/j.icarus.2003.10.010>
- Wentworth, S. J., Keller, L. P., McKay, D. S., & Morris, R. V. (1999). Space weathering on the Moon: Patina on Apollo 17 samples 75075 and 76015. *Meteoritics & Planetary Sciences*, *34*(4), 593–603. <https://doi.org/10.1111/j.1945-5100.1999.tb01366.x>
- Wieczorek, M. A., Weiss, B. P., & Stewart, S. T. (2012). An impactor origin for lunar magnetic anomalies. *Science*, *335*(6073), 1212–1215. <https://doi.org/10.1126/science.1214773>
- Wilhelms, D. E., McCauley, J. F., & Trask, N. J. (1987). The geologic history of the Moon. In *U.S. Geological Survey Professional Paper 1348*.
- Wolfe, E. W., Bailey, N. G., Lucchitta, B. K., Muehlberger, W. R., Scott, D. H., Sutton, R. L., et al. (1981). The geologic investigation of the Taurus-Littrow Valley: Apollo 17 landing site. In *Geological Survey professional. Paper 1080*.
- Xu, S., Poppe, A. R., Harada, Y., Halekas, J. S., & Chamberlin, P. C. (2020). Lunar photoemission yields inferred from ARTEMIS Measurements. *Journal of Geophysical Research: Planets*, *126*(6). <https://doi.org/10.1029/2020JE006790>
- Yan, Q., Zhang, X., Xie, L., Guo, D., Li, Y., Xu, Y., et al. (2019). Weak dust activity near a geologically Young surface revealed by Chang'E-3 mission. *Geophysical Research Letters*, *46*, 9405–9413. <https://doi.org/10.1029/2019GL083611>
- Yeo, L. H., Hood, N., Wang, X., & Horányi, M. (2022). Dust mobilization in the presence of magnetic fields. *Physical Review*, *106*(1), L013203. <https://doi.org/10.1103/PhysRevE.106L013203>
- Zimmerman, M. I., Farrell, W. M., & Poppe, A. R. (2015). Kinetic simulations of kilometer-scale mini-magnetosphere formation on the Moon. *Journal of Geophysical Research: Planets*, *120*(11), 1893–1903. <https://doi.org/10.1002/2015JE004865>